Three-dimensional subwavelength optical imaging using the coupled dipole method

P. C. Chaumet, K. Belkebir, and A. Sentenac
Institut Fresnel (UMR 6133), Université d'Aix-Marseille, Av. Escadrille Normandie-Niemen, F-13397 Marseille Cedex 20, France

(Received 6 November 2003; revised manuscript received 4 March 2004; published 18 June 2004)

We simulate a three-dimensional optical diffraction tomography experiment in which the scattered field from an unknown object is measured for various observation and incident angles. We propose a fast inversion scheme based on the coupled dipole method that enables us to reconstruct the three-dimensional map of permittivity of the object from the far-field data. We show that a power of resolution of $\lambda/4$ can be expected and that the method is robust to noise.

DOI: 10.1103/PhysRevB.69.245405 PACS number(s): 42.30.Wb, 42.25.Fx

I. INTRODUCTION

There has been considerable interest in the development of methods which extend the spatial resolution of optical microscopy beyond the classical diffraction limit and provide information on the three-dimensional structure of the sample. Among their potential applications, one quotes *in-vivo* cell imaging or the optical control of wafers in semiconductor industries.

The existing imaging systems with a resolution smaller than several tens of nanometers, such as atomic force microscopes or optical near-field microscopy,[1] are plagued by the need of approaching a probe in the vicinity (a few nanometers) of the object. Moreover, they are generally limited to surface imaging although, recently, an inversion procedure has been proposed to extract, from the near-field data, the three-dimensional map of permittivity of the sample.[2]

Optical far-field microscopes, on the other hand, permit one to obtain three-dimensional images in a convenient, noninvasive way. Their transverse resolution is limited by the Rayleigh criterion, $\lambda/(2NA)$, where $NA=n\sin\theta$ is the numerical aperture of the objective, with n the index of refraction of the medium surrounding the sample and θ the half-angle of the collection cone of the lenses.[3,4] Enlarging the numerical aperture can be done by immersing the objective in a liquid with a high refractive index or by using a hemispherical prism to collect the scattered light, as in subsurface microscopy.[5] However, the distance of separation of the best microscopes working with visible light and immersed objectives does not exceed 200 nm in the transverse plane and 500 nm in the axial direction.

Optical diffraction tomography (ODT) is another far-field imaging technique that permits one to retrieve the internal structure of semitransparent objects. Although its principles have been established more than 30 years ago,[6] it is only recently that ODT has addressed with success the issue of three-dimensional imaging with subwavelength resolution.[7] It consists of successively illuminating the sample under different directions and collecting the diffracted field for many scattered angles. Then, a numerical inversion procedure is developed to reconstruct the three-dimensional map of permittivity of the sample from the measured data. ODT differs from classic microscopy in that many different illumination configurations are used and that both the phase and amplitude of the scattered field are detected. This last point is the main problem of ODT from an experimental point of view. Indeed, it is very difficult to control the phase of the incident field in an optical experiment, even more so when many different incident directions are required. Yet, under the assumption that the sample does not alter much the transmitted specular beam, it is possible to compensate the noncontrolled incident phase-shift and thus to obtain the absolute phase of the scattered field for all illuminations.[7]

Several elaborate nonlinear inversion schemes have been proposed, mainly in the acoustic and microwave domains, in the simplified case of two-dimensional geometries. These techniques, that account for multiple scattering and incorporate some *a priori* information on the scatterer, may possess a power of resolution smaller than $\lambda/(7NA)$.[8] Yet, their numerical cost is high and their extension to the three-dimensional vectorial problem remains problematic. In this latter case, the few proposed inversion schemes are usually based on Born approximation and they often neglect the vectorial nature of the field.[7,9–11]

In this paper, we simulate an ODT experiment and investigate the power of resolution of the inversion technique. In Sec. II A, we describe briefly the coupled dipole method (CDM) that enables one to calculate the field scattered by a three-dimensional object. In Sec. II B, we propose a fast linear inversion scheme based on the CDM. In Sec. III, we present reconstructions of various objects and study the robustness of the inversion scheme to uncorrelated and correlated noise. Finally, in Sec. IV we conclude on the advantages and drawbacks of our method.

II. THEORY

A. Formulation of the forward scattering problem

The coupled dipole method (CDM) was introduced by Purcell and Pennypacker in 1973 for studying the scattering of light by nonspherical dielectric grains in free space.[12] The object under study is represented by a cubic array of N polarizable subunits. The electromagnetic field at each subunit can be expressed with the following self-consistent equation:

$$\mathbf{E}(\mathbf{r}_i,\omega) = \mathbf{E}^{\mathrm{inc}}(\mathbf{r}_i,\omega) + \sum_{j=1, j\neq i}^{N} \mathbf{T}(\mathbf{r}_i,\mathbf{r}_j,\omega)\alpha(\mathbf{r}_j,\omega)\mathbf{E}(\mathbf{r}_j,\omega), \quad (1)$$

where $\mathbf{E}^{\mathrm{inc}}(\mathbf{r}_i,\omega)$ is the incident field at the position $\mathbf{r}_i$ in the absence of the scattering object, $\mathbf{T}$ is the linear response to a dipole in free space,[13] and $\alpha(\mathbf{r}_j,\omega)$ is the polarizability of the subunit j. As the electromagnetic wave is time harmonic dependent we can omit ω in the expressions. The polarizability is written as

$$\alpha(\mathbf{r}_j) = \frac{\alpha^0(\mathbf{r}_j)}{1 - (2/3)ik^3\alpha^0(\mathbf{r}_j)}, \quad (2)$$

with

$$\alpha^0(\mathbf{r}_j) = \frac{3d^3}{4\pi}\frac{\varepsilon_1(\mathbf{r}_j) - \varepsilon_0}{\varepsilon_1(\mathbf{r}_j) + 2\varepsilon_0}, \quad (3)$$

where d is the spacing of lattice discretization, $\varepsilon_1(\mathbf{r}_j)$ the relative permittivity of the object, and ε_0 and k the relative permittivity and the wave number of the homogeneous medium which contains the object, respectively. The material is isotropic so that $\varepsilon_1(\mathbf{r}_j)$ and the polarizability are scalar. The radiative reaction term in the polarizability, Eq. (2), is important if one wants to compute the optical forces[14–16] or the extinction cross section of an object.[17] But the correction brought by the radiative reaction term, if we are interested only by the scattered field, is small and can be neglected in our study. Hence the polarizability reduces to the Clausius-Mossotti expression, Eq. (3).[18] In that case, for a nonabsorbing object, the polarizability is real.

Once Eq. (1) is solved, the total field scattered by the object at an arbitrary position $\mathbf{r}$ is given by

$$\mathbf{E}(\mathbf{r}) = \mathbf{E}^{\mathrm{inc}}(\mathbf{r}) + \sum_{j=1}^{N} \mathbf{T}(\mathbf{r},\mathbf{r}_j)\alpha(\mathbf{r}_j)\mathbf{E}(\mathbf{r}_j). \quad (4)$$

We can write Eq. (1) in the condensed form

$$\overline{\mathbf{E}} = \overline{\mathbf{E}}^{\mathrm{inc}} + \overline{\overline{\mathbf{A}}}\,\overline{\mathbf{p}}, \quad (5)$$

where the overline on $\overline{\mathbf{E}}$ indicates a vector $3N$ which gathers the electric field at each subunit of the object: $\overline{\mathbf{E}} = [E_x(\mathbf{r}_1), E_y(\mathbf{r}_1), E_z(\mathbf{r}_1), \ldots, E_x(\mathbf{r}_N), E_y(\mathbf{r}_N), E_z(\mathbf{r}_N)]$. $\mathbf{p}(\mathbf{r}_i) = \alpha^0(\mathbf{r}_i)\mathbf{E}(\mathbf{r}_i)$ is the dipole moment of the subunit i and $\overline{\overline{\mathbf{A}}}$ is a square matrix (whose size is $3N \times 3N$) which contains the field tensors susceptibilities $\mathbf{T}(\mathbf{r}_i,\mathbf{r}_j)$.

In an ODT experiment, the scattered field is detected at M observation points for L successive illuminations. Denoting by $\bar{\mathbf{f}}_l$ the vector of the scattered field at each observation points for the lth illumination, we can write the far-field equation, Eq. (4), in the following condensed form:

$$\bar{\mathbf{f}}_l = \overline{\overline{\mathbf{B}}}\,\overline{\mathbf{p}}_l, \quad (6)$$

where $l = 1, \cdots, L$, and $\overline{\overline{\mathbf{B}}}$ is a matrix whose size is $3M \times 3N$. $\overline{\overline{\mathbf{B}}}$ contains the tensors field susceptibilities, $\mathbf{T}(\mathbf{r}_k,\mathbf{r}_j)$ where $\mathbf{r}_j$ denotes a point in the discretized object, $j = 1, \ldots, N$, while $\mathbf{r}_k$ is an observation point, $k = 1, \ldots, M$. Note that $\overline{\overline{\mathbf{B}}}$ does not depend on the angle of incidence.

B. Formulation of the inverse scattering problem

We assume that an unknown object is confined in a bounded box Ω (test domain or an investigating domain) and illuminated successively by $l = 1, \ldots, L$ electromagnetic excitation $\overline{\mathbf{E}}^{\mathrm{inc}}_{l=1,\ldots,L}$. For each excitation l, the scattered field $\bar{\mathbf{f}}_l$ is measured on a surface Γ at M points. The inverse scattering problem is now stated as finding the permittivity distribution ε_1 inside the investigating area Ω such that the associated scattered field matches the measured field $\bar{\mathbf{f}}_{l=1,\ldots,L}$. Many accurate iterative techniques have been developed to solve this inverse problem. In these methods, starting from an initial guess, one adjusts the parameter of interest gradually by minimizing a cost functional involving the measured scattered-field data. Two main approaches can be found in the literature. In the first one,[19–22] the linearized methods, the field in the test domain is considered fixed. This field is the solution of the forward problem, Eq. (5), for the best available estimation of the permittivity at each iteration step, or it is the reference field if the Born approximation is assumed. In the second approach,[23,24] typically the modified gradient method, the field inside the test domain Ω is an unknown that is obtained, together with the permittivity, by the minimization procedure. A hybrid method[25,26] that combines the ideas from the two approaches has also been developed. All these methods deal with two-dimensional inverse scattering problems. In three-dimensions, most techniques use a linear inversion based on Born approximation[9,11] and are restricted to the scalar case. Recently, a more advanced method, namely the contrast source inversion (CSI) method,[27] has been introduced for solving the full vectorial three-dimensional problem.[28,29] In the CSI method the induced dipoles are reconstructed iteratively by minimizing at each iteration step a cost functional involving both the far-field equation, Eq. (6), and the domain-field equation, Eq. (5).

Inspired by the CSI method, we propose in the present paper a simpler iterative scheme. The dipoles are reconstructed using a reduced cost functional involving only the far-field equation. We build up a sequence $\overline{\mathbf{p}}_{l,n}$ according to the following recursive relation:

$$\overline{\mathbf{p}}_{l,n} = \overline{\mathbf{p}}_{l,n-1} + \beta_{l,n}\overline{\mathbf{d}}_{l,n}, \quad (7)$$

where $\overline{\mathbf{d}}_{l,n}$ is an updating direction and will be specified later in the paper. The weighting scalar number $\beta_{l,n}$ is determined at each iteration step by minimizing the cost functional $\mathcal{F}_n$ that represents the discrepancy between the data (measurements) and the scattered field corresponding to the best available estimate of the object $\overline{\mathbf{p}}_{l,n}$. The cost functional $\mathcal{F}_n$ is defined as

$$\mathcal{F}_n(\overline{\mathbf{p}}_{l,n}) = W_\Gamma \sum_{l=1}^{L} \|\bar{\mathbf{f}}_l - \overline{\overline{\mathbf{B}}}\,\overline{\mathbf{p}}_{l,n}\|_\Gamma^2, \quad (8)$$

where W_Γ is a normalizing coefficient,

$$W_\Gamma = \frac{1}{\sum_{l=1}^{L} \|\bar{\mathbf{f}}_l\|_\Gamma^2} \quad (9)$$

and $\|\overline{\mathbf{Q}}\|_\Gamma$ is the deduced norm from the inner product of two vectors $\langle \overline{\mathbf{R}}, \overline{\mathbf{Q}} \rangle_\Gamma$ defined on Γ. This inner product reads as

$$\langle \overline{\mathbf{R}}, \overline{\mathbf{Q}} \rangle_\Gamma = \sum_{\mathbf{r}_k \in \Gamma} \mathbf{R}^*(\mathbf{r}_k) \cdot \mathbf{Q}(\mathbf{r}_k), \tag{10}$$

where $\mathbf{R}^*$ denotes the complex conjugate of $\mathbf{R}$.

Substituting $\overline{\mathbf{p}}_{l,n}$ from Eq. (7) in Eq. (8) leads to a polynomial expression of the weighting coefficients $\beta_{l,n}$. The cost functional $\mathcal{F}_n(\overline{\mathbf{p}}_{l,n})$ is then reduced to a simple cost function $\mathcal{F}_n(\beta_{l,n})$ with respect to L scalar coefficients $\beta_{l,n}$. The minimization is accomplished according to a Polak-Ribière conjugate gradient procedure.[30]

As updating direction $\overline{\mathbf{d}}_{l,n}$ the authors took the Polak-Ribière conjugate gradient direction

$$\overline{\mathbf{d}}_{l,n} = \overline{\mathbf{g}}_{l,n;\mathbf{p}} + \gamma_{l,n} \overline{\mathbf{d}}_{l,n-1}, \tag{11}$$

with

$$\gamma_{l,n} = \frac{\langle \overline{\mathbf{g}}_{l,n;\overline{\mathbf{p}}}, \overline{\mathbf{g}}_{l,n;\overline{\mathbf{p}}} - \overline{\mathbf{g}}_{l,n-1;\overline{\mathbf{p}}} \rangle_\Omega}{\|\overline{\mathbf{g}}_{l,n-1;\overline{\mathbf{p}}}\|_\Omega^2}, \tag{12}$$

where $\langle \cdot, \cdot \rangle_\Omega$ is the same inner product as Eq. (10) but acting on vectors defined on Ω.

The vector function $\overline{\mathbf{g}}_{l;\overline{\mathbf{p}}}$ is the gradient of the cost functional $\mathcal{F}$ with respect to $\overline{\mathbf{p}}_l$ evaluated for the $(n-1)$th quantities. This gradient reads as

$$\overline{\mathbf{g}}_{l,n;\overline{\mathbf{p}}} = W_\Gamma \overline{\overline{\mathbf{B}}}^\dagger [\overline{\mathbf{f}}_l - \overline{\overline{\mathbf{B}}} \overline{\mathbf{p}}_{l,n-1}], \tag{13}$$

where $\overline{\overline{\mathbf{B}}}^\dagger$ is the transpose complex conjugate matrix of the matrix $\overline{\overline{\mathbf{B}}}$.

Once the sources $\overline{\mathbf{p}}_l$ are reconstructed, one can determine the fields $\overline{\mathbf{E}}_l$ inside Ω using Eq. (5). The polarizability α^0 at the position $\mathbf{r}_j$ is then given by

$$\alpha^0(\mathbf{r}_j) = \frac{\sum_{l=1}^{L} \mathbf{E}_l^\star(\mathbf{r}_j) \cdot \mathbf{p}_l(\mathbf{r}_j)}{\sum_{l=1}^{L} |\mathbf{E}_l(\mathbf{r}_j)|^2}. \tag{14}$$

Notice that, if the material under the test is assumed to be without losses, ε_1 is real, the polarizability may be rewritten as

$$\alpha^0(\mathbf{r}_j) = \mathrm{Re}\left\{ \frac{\sum_{l=1}^{L} \mathbf{E}_l^\star(\mathbf{r}_j) \cdot \mathbf{p}_l(\mathbf{r}_j)}{\sum_{l=1}^{L} |\mathbf{E}_l(\mathbf{r}_j)|^2} \right\}. \tag{15}$$

The permittivity ε_1 distribution is determined easily using Eq. (3).

As initial estimate for $\overline{\mathbf{p}}_l$ the authors took the estimate obtained by the back-propagation procedure. This technique is described for the two-dimensional problem in Refs. 26, 31, and 32. The extension to the three-dimensional problem is straightforward and therefore does not need to be presented herein.

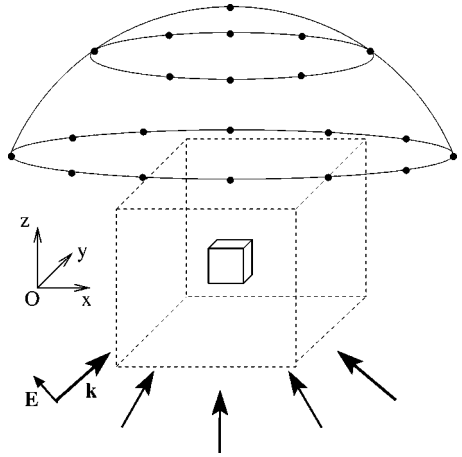

FIG. 1. Sketch of the illumination and detection configuration of the ODT experiment. The points regularly placed on the half sphere are the observation points in far-field.

III. RESULTS

In this section, we simulate an ODT experiment and we present reconstructed maps of permittivity for various objects.

A. Isolated object

We first consider a unique homogeneous object, with relative permittivity ε_1, embedded in a homogeneous medium with relative permittivity ε_0. We define $\varepsilon = \varepsilon_1/\varepsilon_0$ and λ the wavelength in the homogeneous medium.

Figure 1 is a sketch of the experimental configuration. The unknown object is drawn in a plain line while the box in dashed line indicates the domain of investigation taken in the reconstruction procedure. We take $L=31$ incident angles, and $M=65$ observation points. The latter are regularly placed on a half sphere with radius 400 λ, above the (x,y) plane so that one can consider that the scattered field is detected in far-field along 65 directions in a cone of half-angle 80°. Each electromagnetic excitation is a plane wave with wave vector $\mathbf{k}$ belonging to the (x,z) plane with $k_z > 0$. The incident angle with respect to the z-axis θ_i varies from −80° to 80°. In this example, the polarization of the incident electric field lies in the (x,z) plane as shown in Fig. 1. We have done the same study with an incident polarization parallel to the (x,y) plane and obtained very similar results.

The object under study is a cube whose size is $a \times a \times a$ with $a = \lambda/4$, and $\varepsilon = 2.25$. The scattered field at each observation point and for each incident angle is calculated with the CDM [Eqs. (5) and (6)]. The direct problem is solved with a discretization in $N=125$ subunits with width $d = \lambda/20$. Notice that we avoid using the same discretization in the forward and the inverse problems, hence the reconstruction procedure is applied to a test domain discretized into subunits of width $d = \lambda/10$.

Figure 2 shows the maps of the relative permittivity obtained after inversion. In Figs. 2(a), 2(c), and 2(e) the size of the test domain is $1.8\lambda \times 1.8\lambda \times 1.8\lambda$ (6859 subunits) while in Figs. 2(b), 2(d), and 2(f) the size of the test domain is

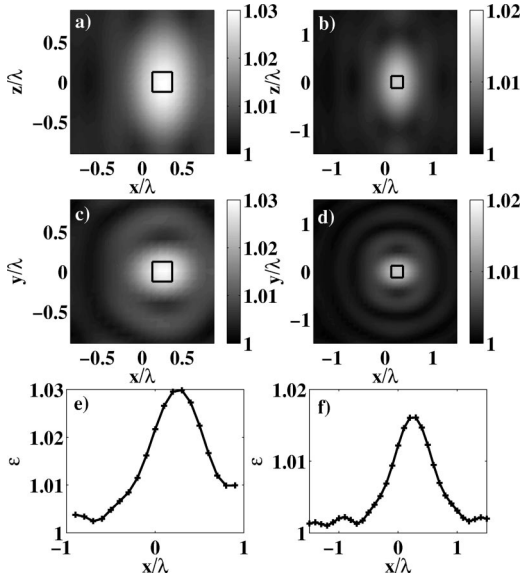

FIG. 2. Reconstructed map of permittivities for two sizes of the test domain. The left side is computed when the size is $1.8\lambda \times 1.8\lambda \times 1.8\lambda$ and the right side when the size is $3\lambda \times 3\lambda \times 3\lambda$. (a) and (b) are the maps of the relative permittivity in the plane (x,z) for $y=0$. (c) and (d) are the maps of the relative permittivity in the plane (x,y) for $z=0$. (e) and (f) are the relative permittivity vs x for $y=z=0$. The bold square indicates the position of the cube.

$3\lambda \times 3\lambda \times 3\lambda$ (29 791 subunits). The center of the cube [indicated by the bold square in Figs. 2(a)–2(d)] is located at $(\lambda/8,0,0)$. The time of computation for the inversion of the smallest problem ($N=6859$ subunits) is less than 7 min on a modern computer (Opteron at 2 GHz). Most of the calculation time (80%) is taken by the resolution of Eq. (5) which permits one to obtain the electromagnetic field from the dipoles in the test domain. This step could be avoided by assuming that the field is close to the incident field, thus resorting to the Born approximation. In this case, the method is close to the singular value decomposition technique presented in Ref. 9. We note that, whatever the size of the box used for the reconstruction, we always localize the position of the object. Yet, the value of the relative permittivity is greatly underestimated and this effect is stronger when the size of the test domain is increased. Indeed, we note that with our simple inversion scheme, the dipoles in the test domain are never equal to zero. Hence we get a kind of "dilution" of the object which reduces the value found for the relative permittivity of the object. To get a physical insight into this phenomenon, we define the "optical volume" of the cube, in analogy with the optical path, as $a^3(\varepsilon-1)$, and we call V the volume of the test domain and $\overline{\varepsilon}$ the average of the relative reconstructed permittivity obtained inside V. When the algorithm's convergence is obtained we find that $V(\overline{\varepsilon}-1)\approx a^3(\varepsilon-1)$. When the volume V increases, $\overline{\varepsilon}$ diminishes and the relative permittivity at the location of the object is lower. This systematic behavior suggests a possible posttreatment to improve the quality of the reconstruction.

If one knows the value of the relative permittivity of the object under study, which is often the case, one can put the values of the weaker dipoles at zero and iterate the process

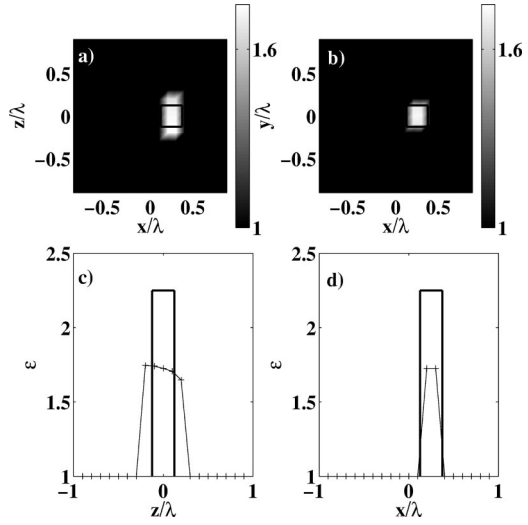

FIG. 3. (a) Map of the relative permittivity in the (x,y) plane $(z=0)$. (b) Map of the relative permittivity in the (x,z) plane $(x=0)$. (c) Relative permittivity vs z for $y=0$, $x=\lambda/8$. (d) Relative permittivity vs x for $y=z=0$.

until the known relative permittivity is reached. In fact this posttreatment amounts to reducing the size of the test domain and permits one to avoid the dilution effect. As the mesh of the test box does not fit exactly the volume of the unknown object, we stop the iterative process when the average of the relative reconstructed permittivity is equal to 0.7ε. Figure 3 shows the images obtained after the posttreatment. We see that in the (x,y) plane [Figs. 3(b) and 3(d)] the object is perfectly localized and the reconstructed shape is close to the real one. On the other hand, the reconstruction of the object deteriorates in the (x,z) or (y,z) plane. This lack of accuracy in the z direction is due to the illumination and collection configuration of our experiment. In transmission diffraction tomography, the incident field comes from below the sample while the detectors are placed above the sample. In this case, the portion of the Ewald sphere that is covered with the far-field data is two times smaller in the axial direction than in the transverse plane.[7] Hence the resolution is twice as large along the z axis than in the (x,y) plane. The same phenomenon is observed with classic optical transmission microscopes. To improve the axial resolution, it is necessary to illuminate and collect the diffracted light from both sides of the sample. This has been done in the 4π microscope[33] and the same resolution is obtained in the transverse and axial directions in that case.

We now study the robustness of our algorithm with respect to noise. We corrupt the scattered far-field data, $\mathbf{f}_{l=1,\ldots,L}$, by an additive uncorrelated noise on each component of the electric field at each position of observation,

$$\tilde{f}_l^{\upsilon}(\mathbf{r}_k) = f_l^{\upsilon}(\mathbf{r}_k) + uAe^{i\phi}, \tag{16}$$

where υ stands for the components along x, y, or z, $A=\max(|\bar{\mathbf{f}}_{l=1,\ldots,L}|)$, and $k=1,\ldots,M$. ϕ is a random number taken for each component of the positions of observation and angles of incidence with uniform probability density in

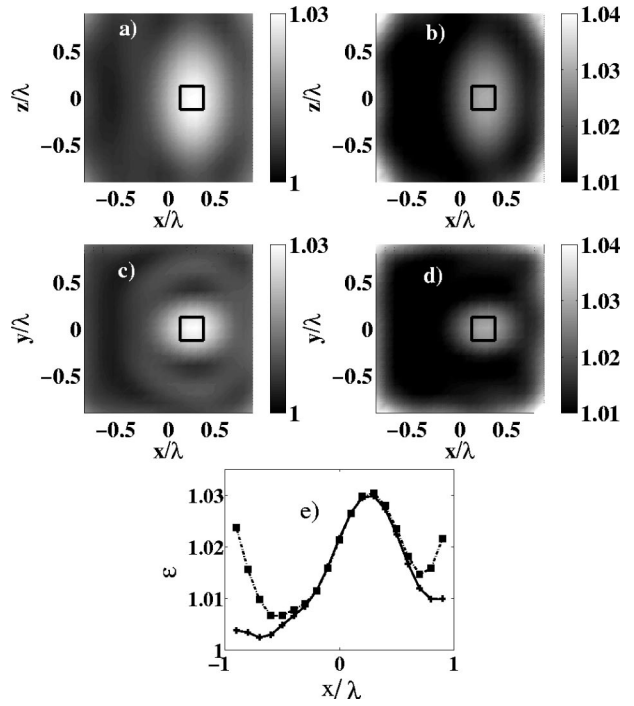

FIG. 4. (a) and (b) map of the relative permittivity in the (x,y) plane at $z=0$. (c) and (d) Map of the relative permittivity in the (x,z) plane at $x=0$. (a) and (c) correspond to $u=0.1$ and (b) and (d) to $u=0.3$. (e) Relative permittivity vs x at $y=z=0$: plain line $u=0$, dashed line with crosses $u=0.1$, and point-dashed line with squares $u=0.3$.

$[0,2\pi]$, and u is a real number smaller than unity that monitors the noise level. We take the same object and the same experimental conditions as those of Figs. 2(a) and 2(c). In Fig. 4 we present the reconstructed map of permittivity in the (x,y) and (x,z) planes for $u=10\%$ and 30%, and in Fig. 4(e) the relative permittivity along the x axis for the three different values of $u=0$ (no noise), 0.1, and 0.3. We note that in Fig. 4(e) the two curves $u=0$ and $u=0.1$ are confounded, and the curves obtained for $u=0.3$ depart from the others only at both extremities of the investigation line. If we look carefully at the map of the relative permittivity, Figs. 4(b) and 4(d), we see that the perturbation due to the noise appears essentially at the edge of the test domain and more particularly at the corner of the box. This behavior is found whatever the size of the investigation box. The perturbation induced by the noise is thus easily eliminated with the posttreatment proposed in Fig. 3 albeit with some precautions. We introduce a second test domain, smaller than the original one, and we apply the regularization only within this second zone. Thus the dipoles located at the edges of the first test domain are never forced to zero. Their role is to absorb the noise so that it does not perturb the second test domain. We finally obtain an image very close to that of Fig. 3. The observed robustness of the inversion scheme must, however, be qualified. Indeed, the noise we have chosen is uncorrelated and can be regarded as a high frequency function added to the scattered amplitudes. Since the far-field data are basically linked to the induced dipoles through a Fourier transform, the noise perturbation will be interpreted as the interference pattern of dipoles as far as possible, i.e., at the extremity of the test domain. Thus the reconstruction of small centered objects is not affected.

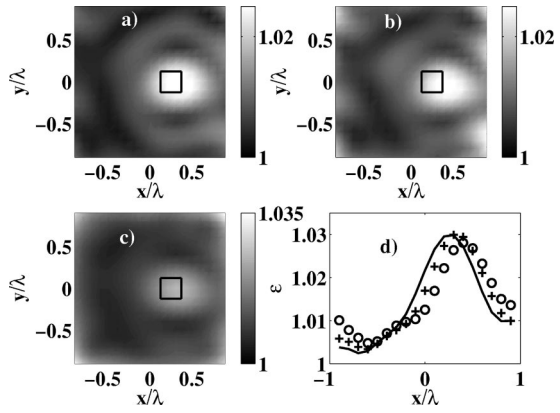

FIG. 5. (a)–(c) Map of the relative permittivity in the (x,y) plane $(z=0)$. (a) $\sigma=0$, $\gamma=\pi/3$. (b) $\sigma=0$, $\gamma=2\pi/3$. (c) $\sigma=\pi/3$, $\gamma=\pi/3$. (d) Relative permittivity vs x for $y=z=0$. Solid line is without noise, crosses correspond to $\gamma=\pi/3$ (a), and circles to $\gamma=2\pi/3$ (b).

Unfortunately, it is most likely that the experimental noise will be correlated. Indeed, due to the envisaged experimental setup, one can expect systematic cumulative errors on the phase measurements as one moves away from the specular direction. We have investigated the behavior of the inversion technique in the presence of correlated noise on the phase, in the form,

$$\tilde{f}_l^v(\mathbf{r}_k) = f_l^v(\mathbf{r}_k)e^{i\psi} \quad \text{with} \quad \psi = \psi_g + \psi_a, \tag{17}$$

where $v=x$, y, or z, $l=1,\ldots,L$, and $k=1,\ldots,M$. ψ_g is a Gaussian noise with mean 0 and standard deviation σ while ψ_a is a correlated noise defined as $\psi_a=(\gamma/2)|\mathbf{k}_d-\mathbf{k}|/|\mathbf{k}|$ where $\mathbf{k}_d$ is the wave vector of the scattered field. In our experimental configuration, Fig. 1, the most important error on the phase, $\max(\psi_a)\approx\gamma$, occurs when $k_{d_x}=-k_x$ and $\theta_i=\pm 80°$.

We observe in Fig. 5(b) that this kind of noise has a small effect on the map of the permittivity, even when the value of the phase error reaches $2\pi/3$ for the furthest directions of observation. In fact, its main effect is to move the location of the object in the x direction, Fig. 5(d). This phenomenon is directly linked to the fact that the object is not at the center of the test box. The second effect is to decrease the value of ε and create some object ghosts. If we add an uncorrelated Gaussian noise, σ, to the correlated noise, we observe in Fig. 5(c) the same behavior as for the white noise previously studied: in addition to the lateral shift, a perturbation at the edge of the test domain appears. Clearly, a correlated noise cannot be eliminated with a simple post-treatment. However, as it stands, the reconstruction scheme is able to provide a rather accurate map of permittivity even with phase errors reaching $2\pi/3$ in certain directions.

B. Many objects

We have also checked the efficiency of the inverse technique when many objects are embedded in the homogeneous

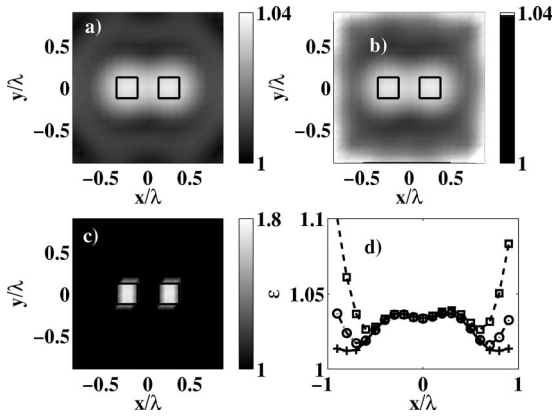

FIG. 6. Two identical cubes ($\varepsilon=2.25$) with $a=\lambda/4$ separated by $\lambda/4$ along the x direction: the center of the first cube is located at $(-\lambda/4,0,0)$ and of second cube at $(\lambda/4,0,0)$. (a)–(c) Map of the relative permittivity in the plane (x,y) with $z=0$. The bold square represents the position of the cubes. (a) Reconstruction with no noise. (b) Reconstruction with 30% of noise. (c) Reconstruction with the regularization used in Fig. 3. (d) Relative permittivity vs x at $y=z=0$: plain line with crosses for $u=0$, dashed line with circles for $u=0.1$, and point-dashed line with squares for $u=0.3$.

medium. If the objects are far from each other, we first take a large test domain with a loose mesh (for example, $d=\lambda/2$) in order to localize the objects. Then, we reduce the domain of investigation to small boxes surrounding every detected site (we can take many separated test domains) and we diminish the spacing of the mesh in each box. This technique is a simple extension of the posttreatment described in the previous section and it can be applied indifferently to objects far apart or close to each other.

To investigate the power of resolution of our imaging system, we take two small cubes of width $a=\lambda/4$ and separated by $\lambda/4$ along the x direction. The conditions of illumination and discretization are the same as those used in Figs. 3–5.

Figures 6(a)–6(c) show the map of the relative reconstructed permittivity in the (x,y) plane at $z=0$ with or without noise and with posttreatment. All the conclusions drawn for an isolated object apply in the case of several objects. First, the perturbation due to the white noise, Eq. (16), appears only at the edge of the investigation box and does not alter the reconstruction of the permittivity. Then, in Figs. 6(a) and 6(b), the two objects are localized, yet the separation between the two cubes is not frankly marked [see Fig. 6(d) plain line with crosses]. Last, if we use the posttreatment, Fig. 6(c), the map of the reconstructed relative permittivity perfectly fits the real shape of the objects in the (x,y) plane. The reconstruction in the (x,y) plane, not shown, displays the same lack of accuracy as that observed in Fig. 3(a). More precisely, we have checked that the resolution is twice as large along the z axis than that along the x axis, by studying the image of two cubes separated by $\lambda/4$ and $\lambda/2$ along the z axis. As expected, we were not able to distinguish the two objects in the first case whereas the separation was clearly visible in the second one.

It is worth noting that the reconstructed image depends on the illumination configuration. In our case the incident beam is varied in the (x,z) plane and the centers of the cubes belong to the x axis. A simple analysis of the portion of the Ewald sphere covered with these illuminations shows that this configuration is the best for obtaining details along the x axis. Indeed, if the plane of incidence is changed to the (y,z) plane, the inversion procedure does not allow one to distinguish the two objects. Now, in general, the orientation of the objects is unknown. Thus the solution consists of illuminating the sample with at least two orthogonal planes of incidence, i.e., the (x,z) and the (y,z) planes. In this case, the separation between the two cubes is less pronounced than that presented in Fig. 6(d) but the posttreatment gives the same maps of permittivity as those presented in Fig. 6(c).

Finally, to investigate further the power of resolution of our technique, we have taken two cubes separated by $\lambda/7$ along the x axis. The inversion procedure, even with the posttreatment, failed to reconstruct the two objects. In this case, it is necessary to implement more sophisticated inversion procedures (such as those developed in 2D[8]).

IV. CONCLUSION

We have simulated a three-dimensional transmission diffraction tomography experiment applied to the optical domain. The inversion algorithm, based on the coupled dipole method, gives the map of permittivity of the object from the far-field amplitudes. This technique does not possess all the refinements of nonlinear inversion procedures but it is simple to implement and its numerical cost is reasonable inasmuch as it does not require one to inverse any matrix. Moreover, it appears quite robust to white noise or phase errors. Taking into account the weakness of the algorithm, we have proposed a posttreatment that significantly improves the images. We show that it is possible to distinguish two objects separated by $\lambda/4$ with relatively few illumination and collection angles. The main interest of this simple inversion technique is its versatility. We intend to extend it to configurations in which the object is placed in the vicinity of a substrate. This can be achieved by adding to the tensor of the free-space susceptibility the tensor of the surface susceptibility.[34] In a more general way if the object is in an environment where we can compute the tensor susceptibility (for example, a multilayer system[35] or a grating[36]) the method presented here can be applied.

ACKNOWLEDGMENTS

This work was supported by a grant of the Ministère de la Recherche, ACI 02 2 0225, and the Conseil Général des Bouches du Rhône and the Conseil Régional PACA. The authors would like to thank Frédéric Forestier for the computer science support.

[1] F. de Fornel, in *Evanescent Waves*, Vol. 73 of Springer Series in Optical Sciences (Springer-Verlag, Berlin, 2001).
[2] P. S. Carney and J. C. Schotland, Appl. Phys. Lett. **77**, 2798 (2000).
[3] O. Haeberlé, C. Xu, A. Dieterlen, and S. Jacquey, Opt. Lett. **26**, 1684 (2001).
[4] J. Enderlein, Opt. Lett. **25**, 634 (2000).
[5] S. B. Ippolito, B. B. Goldberg, and M. S. Ünlü, Appl. Phys. Lett. **78**, 4071 (2001).
[6] E. Wolf, Opt. Commun. **1**, 153 (1969).
[7] V. Lauer, J. Microsc. **205**, 165 (2002).
[8] K. Belkebir and A. Sentenac, J. Opt. Soc. Am. A **20**, 1223 (2003).
[9] P. S. Carney, V. A. Markel, and J. C. Schotland, Phys. Rev. Lett. **86**, 5874 (2001).
[10] E. Wolf, Opt. Commun. **1**, 153 (1969).
[11] S. Kawata, O. Nakamura, and S. Minami, J. Opt. Soc. Am. A **4**, 292 (1987).
[12] A. M. Purcell and C. R. Pennypacker, Astrophys. J. **186**, 705 (1973).
[13] J. D. Jackson, *Classical Electrodynamics*, 2nd ed. (Wiley, New York, 1975).
[14] P. C. Chaumet and M. Nieto-Vesperinas, Phys. Rev. B **61**, 14 119 (2000).
[15] P. C. Chaumet and M. Nieto-Vesperinas, Phys. Rev. B **62**, 11 185 (2000).
[16] P. C. Chaumet and M. Nieto-Vesperinas, Opt. Lett. **25**, 1065 (2000).
[17] B. T. Draine, Astrophys. J. **333**, 848 (1988).
[18] A. Lakhtakia, Int. J. Mod. Phys. C **3**, 583 (1992).
[19] W. C. Chew and Y. M. Wang, IEEE Trans. Med. Imaging **9**, 218 (1990).
[20] N. Joachimowicz, C. Pichot, and J.-P. Hugonin, IEEE Trans. Antennas Propag. **39**, 1742 (1991).
[21] A. G. Tijhuis, Wave Motion **11**, 151 (1989).
[22] A. G. Tijhuis, K. Belkebir, A. C. S. Litman, and B. P. de Hon, IEEE Trans. Geosci. Remote Sens. **39**, 1316 (2001).
[23] R. E. Kleinman and P. M. van den Berg, J. Comput. Appl. Math. **42**, 17 (1992).
[24] R. E. Kleinman and P. M. van den Berg, Radio Sci. **28**, 877 (1993).
[25] K. Belkebir and A. G. Tijhuis, Inverse Probl. **17**, 1671 (2001).
[26] K. Belkebir, S. Bonnard, F. Pezin, P. Sabouroux, and M. Saillard, J. Electromagn. Waves Appl. **14**, 1637 (2000).
[27] P. M. van den Berg and R. E. Kleinman, Inverse Probl. **13**, 1607 (1997).
[28] A. Abubakar, P. M. van den Berg, and B. J. Kooij, IEICE Trans. Electron. **E83-C**, 1864 (2000).
[29] A. Abubakar and P. M. van den Berg, Inverse Probl. **18**, 495 (2002).
[30] W. H. Press, B. P. Flannery, S. A. Teukolski, and W. T. Vetterling, *Numerical Recipes: The Art of Scientific Computing* (Cambridge University Press, Cambridge, England, 1986).
[31] L. Souriau, B. Duchêne, D. Lesselier, and R. E. Kleinman, Inverse Probl. **12**, 463 (1996).
[32] R. E. Kleinman and P. M. van den Berg, Radio Sci. **29**, 1157 (1994).
[33] M. Schrader and S. Hell, J. Appl. Phys. **84**, 4033 (1998).
[34] P. C. Chaumet, A. Rahmani, F. de Fornel, and J.-P. Dufour, Phys. Rev. B **58**, 2310 (1998).
[35] A. Rahmani, P. C. Chaumet, and F. de Fornel, Phys. Rev. A **63**, 023819 (2001).
[36] P. C. Chaumet, A. Rahmani, and G. W. Bryant, Phys. Rev. B **67**, 165404 (2003).